

# Molecular Dynamics Prediction of the Effect of Neutron Irradiation on the Ductile-to-Brittle Transition in Fe–Ni–Cr Alloys

A. Ustrzycka<sup>a,\*</sup>, H. Mousavi<sup>a</sup>, F. J. Dominguez-Gutierrez<sup>b</sup> and S. Stupkiewicz<sup>a</sup>

<sup>a</sup>*Institute of Fundamental Technological Research, Polish Academy of Sciences, Pawinskiego 5B, Warsaw, 02-106, Poland*

<sup>b</sup>*NOMATEN Centre of Excellence, National Centre for Nuclear Research, ul. A. Soltana 7, Otwock, 05-400, Poland*

---

## ARTICLE INFO

### Keywords:

DBT  
Radiation-induced defects  
MD simulations  
Crack propagation  
Critical strain energy release rate  
Cr-rich alloys

## ABSTRACT

This study provides a comprehensive investigation into the fracture behavior of irradiated Fe–Ni–Cr alloys, focusing on the radiation-induced ductile-to-brittle transition (DBT). Unlike the commonly studied temperature-driven DBT, this transition is driven by radiation-induced defects, which impede dislocation motion and reduce the material's capacity for plastic deformation, ultimately leading to brittle failure. Utilizing Molecular Dynamics simulations, this work examines the interaction between radiation-induced defects, such as dislocation loops and voids, and their influence on crack propagation and energy dissipation mechanisms. The results reveal distinct roles played by these defects: voids facilitate crack growth by reducing local cohesive energy, while dislocation loops act as barriers that impede crack advancement and redirect crack paths, significantly altering crack morphology. Building on the classical approach of separating fracture energy into brittle cleavage and plastic components, this study adapts this decomposition to irradiated materials. This approach appraises the distinct roles of surface energy and plastic work across varying radiation damage levels, providing critical insights into how irradiation-induced defects govern fracture dynamics.

---

## 1. Introduction

The embrittlement of metals, resulting from reduced plastic deformation preceding fracture, is a significant determinant of the durability and safety of structural materials, particularly under the extreme conditions encountered in nuclear reactors. Irradiation embrittlement plays a crucial role in the degradation of the mechanical properties of these materials. Radiation defects arise when energetic particles, such as neutrons or ions, collide with atoms in the lattice, displacing them from their original positions and creating vacancies and interstitial atoms, which subsequently cluster into more complex defect structures such as dislocations and voids [1–4].

In irradiated materials, ductile-to-brittle transition (DBT) is driven by radiation defects, which impede dislocation motion and reduce the material's capacity for plastic deformation, ultimately leading to a brittle failure.

DBT is a well-known phenomenon in metals that is usually related to the temperature sensitivity of fracture stress and yield stress [5–8]. DBT is characterized by a shift from ductile fracture, which involves significant plastic deformation, to brittle fracture, where materials fail with little prior deformation [9, 10]. This transition is heavily influenced by temperature, stress state, and microstructural factors, particularly the presence of defects. While temperature is recognized as an important factor in the overall understanding of DBT phenomenon, the accumulation of radiation-induced defects and their influence on mechanical properties are considered the determining elements in the case of irradiated materials.

---

ORCID(s):

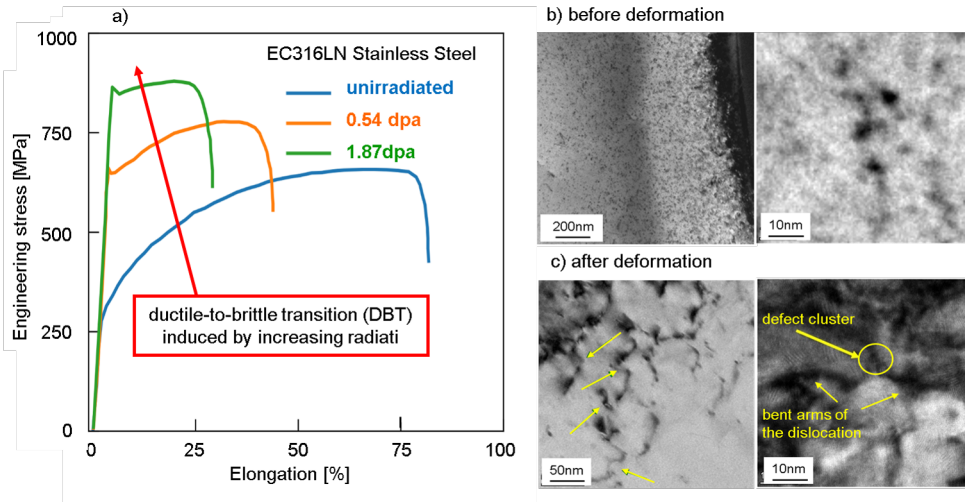


**Figure 1:** a) Engineering stress–strain curves of stainless steel after irradiation, demonstrating ductile-to-brittle transition (after Byun et al. [11]). b) Transmission electron microscopy (TEM) analysis of steel irradiated to 0.12 dpa, showing radiation-induced porosity in the form of defect clusters at varying magnifications [12]. c) TEM images illustrating the dislocation-blocking mechanism, where a dislocation line encircles radiation defects at varying magnifications [12]. These images depict the irradiated material after deformation, highlighting the interaction between dislocations and radiation-induced defects.

Fig. 1 illustrates the impact of irradiation on the mechanical behavior of stainless steel. The stress–strain curves demonstrate the reduction of ductility with increasing radiation-induced porosity (compare Fig. 1a). The curves clearly show a decrease in elongation at fracture with higher radiation doses, indicating a significant loss of plasticity. This loss of ductility is directly related to the increase of radiation porosity and defect accumulation. The reduction of ductility is a critical factor contributing to ductile–brittle transition (DBT). As shown in Fig. 1b), irradiation-induced defects such as voids and dislocation loops form clusters that disrupt the crystalline structure, impeding the material’s ability to deform plastically [12–14]. Additionally, TEM images in Fig. 1c) reveal the dislocation-blocking mechanism, where dislocation lines bend and encircle radiation defects, forming curved arms. This interaction, observed after deformation, significantly restricts plastic flow by impeding dislocation motion [15–18]. These microstructural changes, driven by the accumulation of defects, significantly degrade the mechanical integrity of the material under applied stress. Thus, defect accumulation can play a pivotal role in driving DBT.

Molecular dynamics (MD) simulations play a critical role in studying DBT by providing atomic-level insights into the mechanisms driving embrittlement [19, 20]. In the case of irradiated materials, MD allows for detailed investigation of radiation-induced defects and their interactions with crack propagation and dislocation motion [14, 15, 17, 18, 21–23]. These simulations are particularly useful for examining the effects of radiation defects on material behavior, enabling the exploration of how defect accumulation changes the mechanical properties of the materials [16, 17]. MD can simulate extreme irradiation conditions and provide a clear understanding of the transition from ductile to brittle fracture at various defect densities.

This paper presents a novel investigation into the role of radiation-induced defects, expressed by the displacement per atom (dpa) parameter [4], in driving the ductile-to-brittle transition. Unlike previous studies, which primarily focus on temperature-driven DBT, this work examines the direct influence of irradiation-induced defects on dislocation dynamics and energy dissipation mechanisms during crack propagation. By systematically analyzing how varying dpa levels govern defect accumulation and alter the material’s capacity for plastic deformation, this study establishes a direct link between irradiation damage

and fracture behavior, an aspect that has not been comprehensively addressed before. Furthermore, this paper provides the first detailed correlation between defect density and the microstructural mechanisms governing DBT. Through a combination of MD simulations and advanced defect characterization techniques, this study offers original insights into how variations in dpa influence the mechanical response, including the transition from ductile to brittle fracture.

A comprehensive understanding of DBT phenomenon in irradiated materials is crucial for accurately predicting material performance in nuclear applications and for devising effective strategies to mitigate embrittlement effects. Understanding the fracture behavior of irradiated structural materials is essential to ensuring the safety and reliability of structural components of nuclear reactors operating in exceptionally harsh environments due to the combination of high stresses, a chemically aggressive coolant, high or, in the case of the accelerator system, extremely low temperatures, and intense radiation fluxes [22, 24–27].

The paper is organized as follows: Section 2 outlines the simulation methodology and the MD framework for modeling irradiated alloys, including the preparation of irradiated samples, characterization of defect densities, and simulations of fracture behavior. This section focuses on the physical mechanisms underlying defect-crack interactions, including dislocation emission and crack tip shielding, to elucidate how irradiation alters fracture pathways and energy dissipation. Section 3 explores the micro-mechanisms governing DBT in irradiated materials, emphasizing the role of radiation-induced defects in altering dislocation dynamics and crack propagation. Section 4 introduces the decomposition of fracture energy into cleavage and plastic contributions to quantify the energy dissipation during fracture in irradiated materials.

## 2. Simulation methodology

### 2.1. Preparation of the irradiated samples

The methodology employed for samples irradiation closely follows procedures established in our earlier papers [12, 28–30] and is only briefly summarized here. To investigate the formation and evolution of dislocations and voids under various dpa values, MD simulations were performed using the Large-scale Atomic/Molecular Massively Parallel Simulator (LAMMPS) software [31].

The interatomic potential used for these simulations was developed by Bonny et al. [32, 33] based on the Embedded Atom Method (EAM) with Ziegler-Biersack-Littmark (ZBL) corrections. This potential is well-suited for modeling defect formation and short-range interactions in face-centered cubic (fcc) materials, offering reliable predictions of dislocation behavior and stacking fault energies (SFEs) over a broad temperature range of 0–900 K for Fe–Ni–Cr alloy structures [12, 30, 34, 35].

For this study, a Cr-rich fcc  $\text{Fe}_{55}\text{Ni}_{19}\text{Cr}_{26}$  sample with dimensions of  $137.5 \times 141.0 \times 148.0 \text{ \AA}^3$  was prepared containing 262 080 atoms. The composition  $\text{Fe}_{55}\text{Ni}_{19}\text{Cr}_{26}$  represents the atomic percentage of each element, and the sample was oriented along the  $\langle 001 \rangle$  crystallographic direction. The irradiation of samples for a wide range of dpa was achieved through overlapping collision cascade simulations [3, 4, 12]. Each cascade was initiated by a primary knock-on atom (PKA) with an energy of 10 keV, randomly selected within the simulation box to ensure uniform damage distribution.

For example, to achieve dpa values of 0.008, 0.038, 0.152, and 0.266, as shown in Fig. 2; 20, 100, 400, and 700 consecutive recoil MD simulations were performed, respectively. Each recoil event was simulated for 20 ps under the NPT ensemble, followed by an additional 10 ps to allow for stress relaxation and swelling [12]. Defect formation, including dislocation nucleation and void generation, was analyzed across various dpa levels using the Dislocation Extraction Algorithm (DXA) in OVITO [36]. Dpa dose was calculated using the model proposed by Nordlund et al. [4].

The evolution of the density of radiation-induced dislocation loops and voids, as functions of the irradiation dose, are shown in Fig. 3a) and Fig. 3b), respectively. The density of radiation defects increases

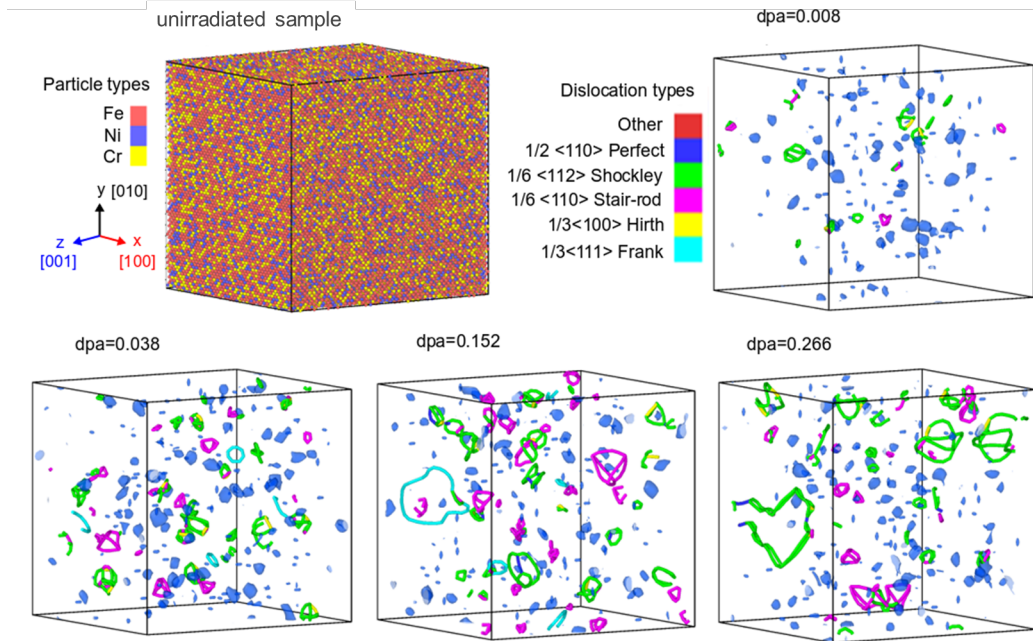


**Figure 2:** Structural evolution of radiation defects in Fe-Ni-Cr Alloy with increasing dpa. The legend identifies the types of dislocation loops and their designations. Voids are represented in blue.

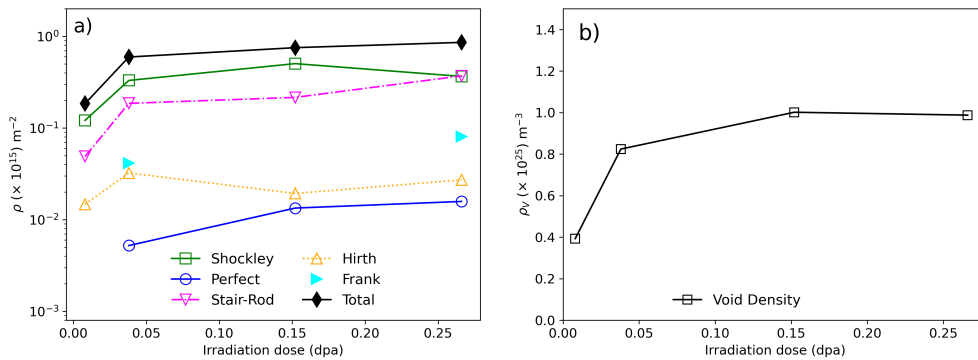


**Figure 3:** Dislocation loops (a) and voids density (b) as a function of the irradiation dose in dpa obtained from MD simulations.

gradually at lower dpa, reflecting the early stages of dislocation loop nucleation and the initial aggregation of vacancies into stable void structures. At higher dpa levels, the accumulation and interaction of dislocations lead to the formation of various dislocation types and a more complex defect network. Fig. 2 provides a detailed depiction of how microstructural features, including dislocation loops and void densities, evolve under increasing radiation exposure, highlighting the transition from isolated defects to a dense defect structure.

## 2.2. Simulations of fracture

A three-dimensional (3D) atomic-scale model shown in Fig. 4 was prepared to enable the simulation and analysis of fracture mechanics phenomena. The irradiated samples obtained from the irradiation step (Section 2.1) were duplicated using periodic replication techniques along the x- and y- axes to achieve the

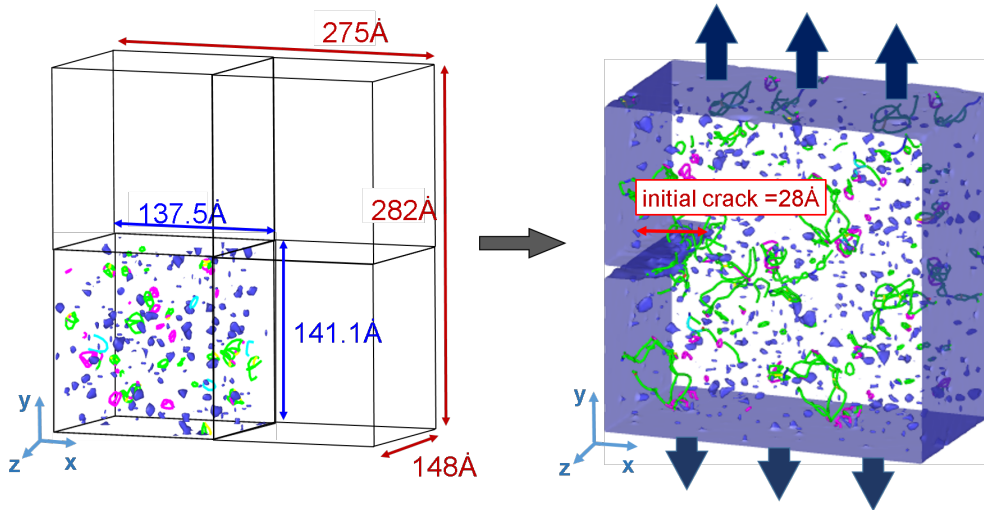


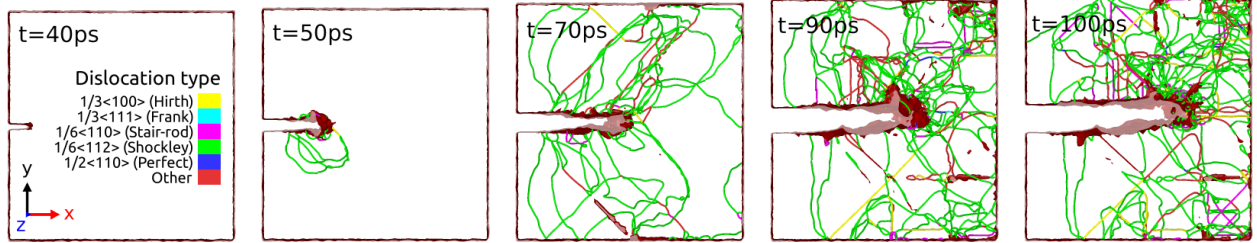
**Figure 4:** Schematic representation of the 3D atomic-scale fracture model. The simulation box prepared by replicating an irradiated sample along the x- and y-axes is shown on the left side. The model with an initial crack introduced at the midplane subjected to uniform elongation is shown on the right side.

desired model dimensions of  $275 \times 282 \times 148 \text{ \AA}^3$ . The simulation box, containing 1 048 320 atoms, provides a sufficient volume to capture crack-related phenomena without significant boundary interference. To ensure the stability of the fracture model under the specified conditions, a relaxation step was performed for 10 ps following an equilibration process using a canonical NPT ensemble for 100 ps at a target temperature of 300 K and zero stress. This equilibration phase allowed both atomic positions and simulation box dimensions to adjust dynamically, ensuring the system reached a stable thermodynamic state. Following equilibration, the NVT ensemble was applied to preserve a constant temperature throughout the deformation process, ensuring thermal stability and eliminating artifacts such as unintended energy dissipation or volume fluctuations that might influence crack propagation behavior. An initial crack with a length of 28 Å was then introduced at the midplane of the specimen by selectively removing the bonds between atoms along the x-axis to create a sharp discontinuity.

Due to the low thickness of the crystal compared to its height and width, this problem is modeled as a constrained 3D system [2]. Periodic boundary conditions are applied along the thickness of the crystal (i.e., z-direction), while non-periodic boundary conditions are used in the x- and y-directions, corresponding to the crack propagation and loading direction, respectively. To prevent necking and minimize residual effects (unwanted structural deformations), the atoms at the left and right edges of the sample (see Fig. 4) are restricted from moving in the x-direction but remain free to move along the y- and z-axes, in accordance with the assumed potential and loading conditions. In addition, two atomic layers at the top and bottom of the sample along the y-direction are kept frozen. The system is subjected to uniform elongation along the y-direction, applied to the upper and lower boundaries. The displacement rate is set to 0.08 Å/ps, corresponding to a global strain rate of  $10^9 \text{ 1/s}$ . Several alternative boundary condition configurations, such as fully periodic (ppp) [38] or fully free (ffp) and non-periodic with shrink-wrapped (ssp) [2, 6, 20, 39] systems, were also tested. However, in the case of (ffp) and (ssp) conditions, excessive necking of the sample occurred due to its high ductility, severely distorting the plastic zone and obscuring the underlying fracture mechanisms. On the other hand, (ppp) configurations artificially modify plastic flow near the crack front due to the interaction of dislocations with periodic boundary conditions, which create virtual copies of the sample that influence the dislocation fields. Therefore, the constrained boundary setup used in this work was selected as a compromise

## Ductile-to-Brittle Transition

pristine sample



sample irradiated to 0.152 dpa

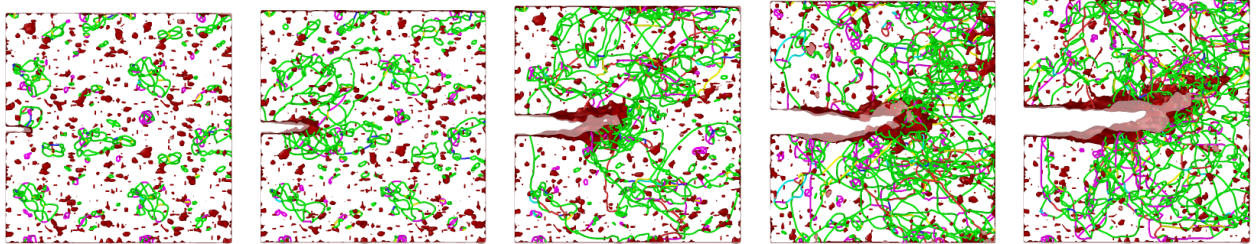
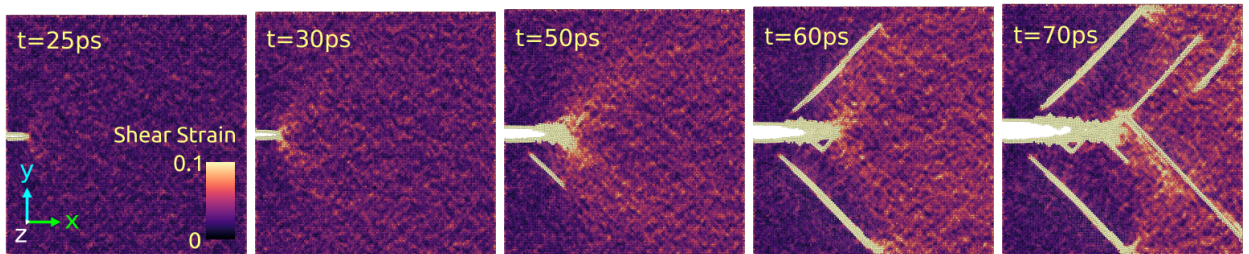


**Figure 5:** Crack propagation for non-irradiated and irradiated sample.

that preserves realistic plasticity and dislocation behavior while preventing unphysical deformation modes. Following the criteria established by Buehler [40], a time step of 1 fs is used for the simulations. This approach provides the foundation for analyzing the mechanical response and fracture behavior of both unirradiated and irradiated samples.

The crack propagation in both a unirradiated sample and in a selected irradiated sample (0.152 dpa) is illustrated in Fig. 5, where the role of radiation-induced defects on dislocation behavior and crack path

unirradiated sample



sample irradiated to 0.152 dpa

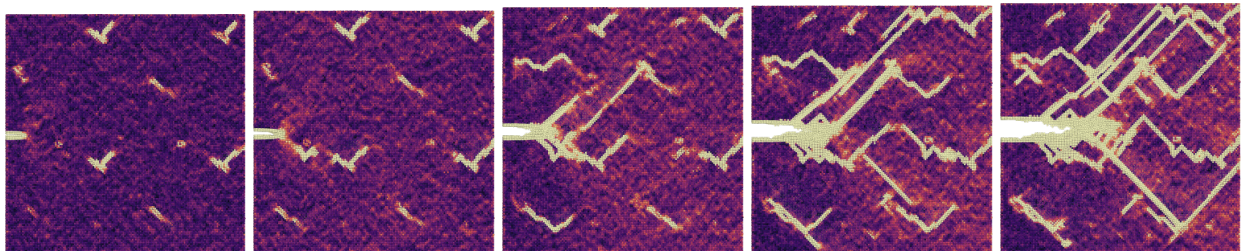


**Figure 6:** Equivalent shear strain fields calculated using the Green–Lagrangian strain tensor [37] in a selected cross-section of unirradiated and irradiated samples.

characteristics is highlighted. In the pristine sample, crack growth generates significant dislocation activity near the crack tip, dissipating energy through plastic deformation and effectively blunting the crack tip.

However, in the irradiated sample, the presence of radiation-induced defects modifies dislocation dynamics, disrupting the characteristic mechanisms of energy dissipation through plastic deformation. Fig. 6 presents shear strain fields in both unirradiated and irradiated samples across various time steps. Using the Green–Lagrangian strain tensor, the local shear strain is computed, and these scalar quantities are output as particle properties [37, 41]. The images show clear differences in strain localization patterns, where the irradiated samples exhibit concentrated strain fields at radiation-induced defects.

### 3. Characterization of mechanisms governing crack propagation in irradiated materials

In irradiated materials, crack propagation is profoundly influenced by the density, type, and spatial distribution of radiation-induced defects. These defects act as obstacles to dislocation motion, modifying the local stress fields around the crack and restricting the material's ability to dissipate mechanical energy through plastic deformation. As a result, the crack path can be redirected, with propagation either hindered or accelerated depending on the nature and arrangement of the defects. To investigate these effects, the crack evolution at different irradiation levels is analyzed, focusing on crack morphology, and interactions with radiation-induced defects.

In the following subsections, various modes of crack propagation in irradiated materials are examined in detail. Subsection 3.1 examines characteristic modes of crack growth, highlighting how radiation-induced defects alter crack trajectories and lead to phenomena such as crack branching, void coalescence, and secondary crack formation. Subsection 3.2 delves into the fundamental mechanisms governing defect–crack interactions, focusing on how specific defects (e.g., voids, dislocation loops, rigid inclusions) either facilitate or impede crack propagation and how these interactions influence fracture behavior.

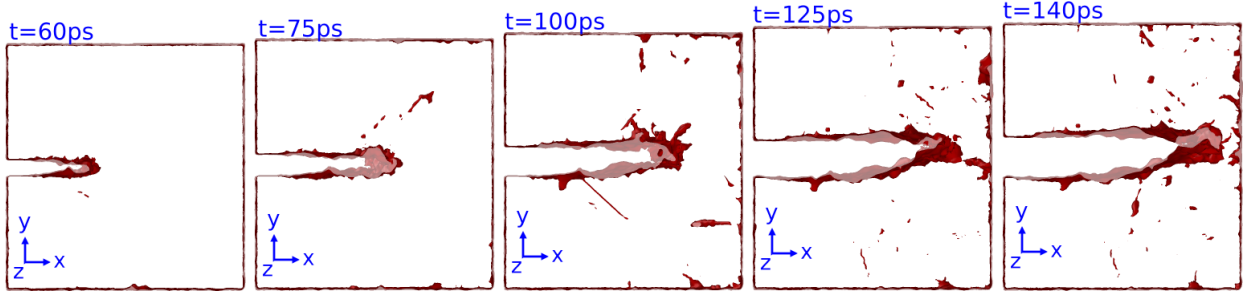
#### 3.1. Characteristic modes of crack growth in irradiated structures

In this subsection, representative cases are examined to show the complex mechanisms driving crack evolution under irradiation. Fig. 7 illustrates the crack propagation process in both unirradiated and irradiated samples.

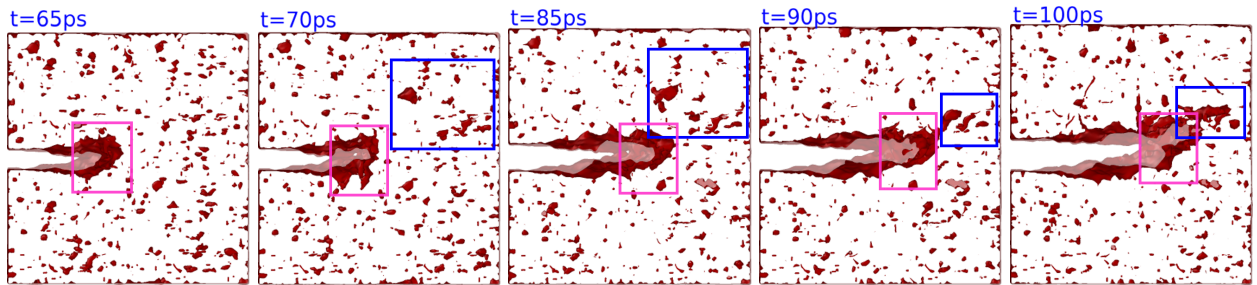
In the unirradiated sample (top row of Figs 5 and 7), the crack advances with minimal resistance, exhibiting a relatively smooth growth path accompanied by a developed plastic zone at the crack tip. The emission of dislocations near the crack tip is observed to hinder crack propagation by redistributing stress and promoting localized plastic deformation. This dislocation activity contributes to crack tip blunting (Fig. 7: at 75 to 100 ps), as evidenced by the gradual widening of the crack tip and the formation of a diffuse plastic zone (Fig. 5: at 70 to 100 ps).

In the irradiated samples, the crack growth dynamics is distinctly different. The sample with 0.152 dpa (Fig. 7: middle row) shows a crack path that is restricted and/or redirected under the influence of radiation-induced defects. The crack path is altered by the presence of radiation-induced defects, which act as local strain concentrators. These defects intensify dislocation emission and change the crack propagation behavior. Unlike the unirradiated sample in Fig. 5, where dislocations are primarily emitted from the crack tip, the irradiated sample exhibits additional dislocation activity originating from radiation-induced defects (Fig. 5, sample irradiated to 0.152 dpa). These defects not only concentrate strain and contribute to higher dislocation density but also limit the mobility of the emitted dislocations, thereby restricting plastic deformation and modifying the crack's trajectory. As a result, an amorphous zone with a varying width of 2–5 nm is formed at the crack tip (in Fig. 7, marked with a pink frame). The zone evolves dynamically, propagating together with the crack tip.

unirradiated sample



sample irradiated to 0.152 dpa



sample irradiated to 0.266 dpa

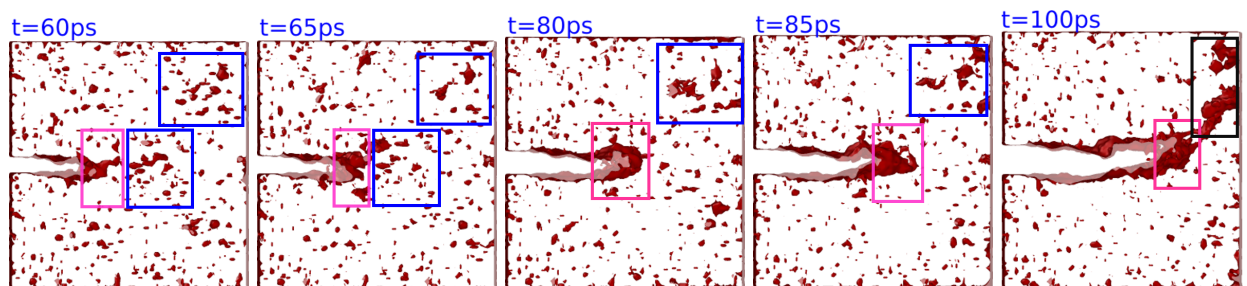


**Figure 7:** Influence of radiation-induced voids and dislocation obstacles on crack growth paths. The coalescence of voids is highlighted with a blue frame, the amorphous zone with a pink frame, and the formation of secondary cracks with a black frame.

Furthermore, under mechanical loads, as the crack advances, radiation-induced voids expand and coalesce, forming larger void structures. The blue frames in Fig. 7 highlight instances where previously isolated voids join together. This coalescence is driven by localized plastic deformation, which facilitates void merging and provides an easier path for crack propagation. Notably, this mechanism is analogous to void coalescence observed in non-irradiated ductile materials [42]. Near the crack tip, coalescing voids create additional weak zones, directing the crack toward areas of lower resistance. This process enhances crack branching and influences its overall morphology. Eventually, as the crack encounters clusters of coalesced voids, these merged structures integrate into the main crack, leading to more irregular and complex crack propagation patterns (Fig. 7; at 100 ps).

In the sample irradiated to 0.266 dpa (Fig. 7; bottom row), the crack propagation is on the one hand blocked by the dense defect field, leading to the formation of an amorphous zone at the crack tip (marked with a pink frame), on the other hand, the crack propagation is promoted by the coalescence of voids at the crack tip (marked with a blue frame). In addition, a secondary crack begins to form on the opposite side (Fig. 7; at 100 ps, marked with a black frame), initiating around radiation-induced voids. The development

sample irradiated to 0.07 dpa

t=5ps

t=10ps

t=30ps

t=40ps



sample irradiated to 0.494 dpa

t=5ps

t=10ps

t=25ps

t=40ps

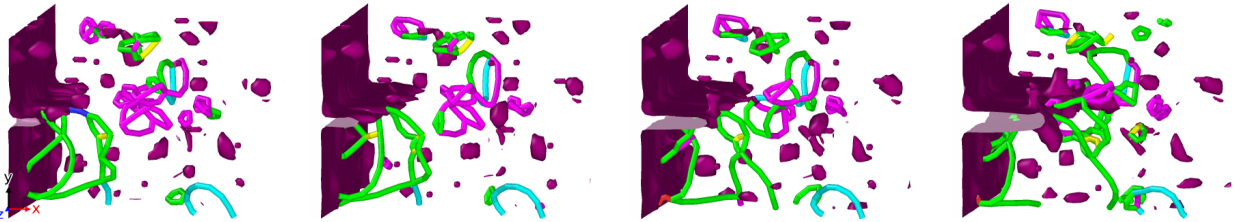


**Figure 8:** Interaction between the crack tip and radiation-induced defects. The colors representing different defect types are explained in the legend of Fig. 5.

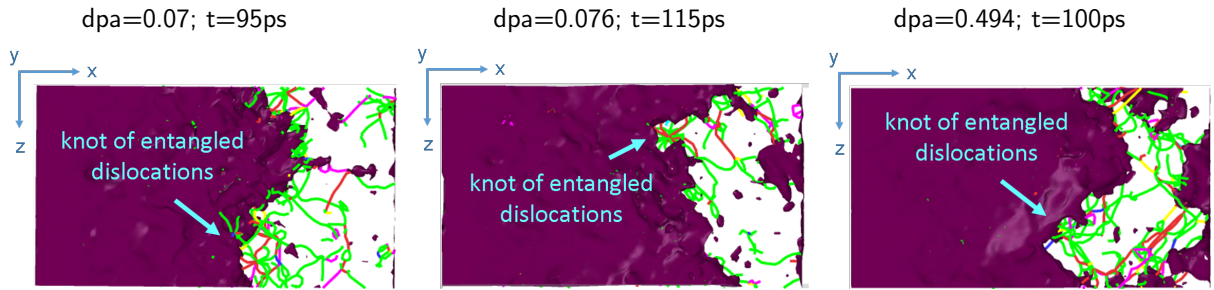
of this secondary crack is also driven by the coalescence of voids (marked with a blue frame), which create weak regions that facilitate crack initiation and propagation. Eventually, the primary and secondary cracks merge, resulting in a more complex crack path.

Fig. 7 reveals the dynamic interaction between crack progression and void evolution, demonstrating how void growth, void coalescence, and subsequent merging with the crack enhance crack propagation. Moreover, Fig. 7 discloses that in irradiated materials, secondary cracks can form if the stress level in the sample is sufficiently high and the primary crack is blocked by tangled dislocations or amorphous zones. When radiation voids develop and coalesce in other regions of the material, these zones become weakened and may serve as initiation sites for secondary cracks. This process ultimately leads to a complex fracture morphology that is significantly influenced by void accumulation and absorption.

Fig. 8 shows the interaction between the crack front and radiation defects at the early stage. In regions with high void concentrations (Fig. 8; sample irradiated to 0.07 dpa; top row), cracks can propagate more easily as the local lattice structure is weakened. The presence of radiation voids lowers effectively the cohesive energy, making the material more susceptible to crack initiation under mechanical loading [43]. As the crack propagates through regions with high concentrations of vacancy clusters, its growth is accelerated due to the reduced local resistance to fracture (Fig. 8; sample irradiated to 0.07 dpa; top row). The crack tip grows through the space previously occupied by the void.

Another critical mechanism that influences crack growth and changes the material's fracture behavior is the interaction between a propagating crack and radiation-induced dislocation loops (Fig. 8; sample irradiated to 0.494 dpa). The radiation-induced dislocation loops act as barriers to dislocation motion, reducing dislocation mobility near the crack tip. When the crack encounters a dislocation loop, the loop obstructs further dislocation propagation and creates local zones of high resistance (Fig. 8; sample irradiated to 0.494 dpa; at 40 ps).

## Ductile-to-Brittle Transition



**Figure 9:** Clustering of radiation-induced dislocation loops near the crack front. The burgundy color indicates a cross-section of the crack in the x-z plane, highlighting a cross-sectional view of the crack.

These mechanisms analysis highlight how voids and loops exert contrasting effects on crack behavior, with voids accelerating propagation and dislocation loops impeding it. For instance, radiation-induced dislocation loops can cluster near the crack front, forming a knot of entangled dislocations that further complicates the crack propagation process. In this case, the crack's progress is slowed or halted as it encounters this dense, immobile cluster of dislocations. This mechanism is shown in Fig. 9 for different values of dpa at selected time instants. This structure acts as a strong inclusion that prevents further crack advancement, effectively blocking the crack path. The accumulated loops at the crack tip serve as a physical barrier that limits crack propagation by restricting dislocation mobility. In higher-dpa samples, secondary cracks can form as they initiate on the radiation defects, where the critical energy for atomic bond breaking is reached due to stress concentrations (see Fig. 7). This behavior illustrates a transition toward crack branching, where the main crack's path is impeded, leading to the initiation and coalescence of secondary cracks that eventually merge with the main crack. This phenomenon, driven by high defect density, can contribute to the complex fracture patterns seen in highly irradiated materials [44–46].

### 3.2. Fundamental mechanisms governing defect–crack interactions

The interaction between radiation-induced defects and propagating cracks plays a pivotal role in defining the fracture behavior of irradiated materials. While previous sections explored the broad impact of irradiation on crack propagation dynamics and the microstructural changes induced by defects, this subsection focuses on analyzing specific, fundamental interactions between individual defects and a crack front.

Fig. 10 captures representative cases of defect–crack interactions, showcasing how different defect types—small voids, large voids, dislocation loops, and rigid inclusions—influence crack morphology and behavior. Each row of Fig. 10 corresponds to a distinct scenario, selected for its ability to illustrate the diversity of interactions and their implications for crack propagation. By isolating these mechanisms, the physical principles governing crack evolution under varying microstructural conditions and irradiation levels are revealed.

The analysis highlights how certain defects, such as voids, act as facilitators for crack growth by reducing effective cohesive energy, while others, like dislocation loops and rigid inclusions, serve as barriers that redirect or even halt crack progression. These analysis provides a deeper understanding of how microstructural features influence crack dynamics and fracture patterns.

To investigate these interactions, simulations were conducted using a sample with dimensions of  $275 \times 282 \times 148 \text{ \AA}^3$ , consistent with the setup described in Section 2.2. The defects were designed to reflect their typical geometries as observed in experiments: small voids with a diameter of 2.5 nm, large voids with a diameter of 5 nm, dislocation loops spanning 5 nm, and rigid inclusions with diameter of 5 nm. These

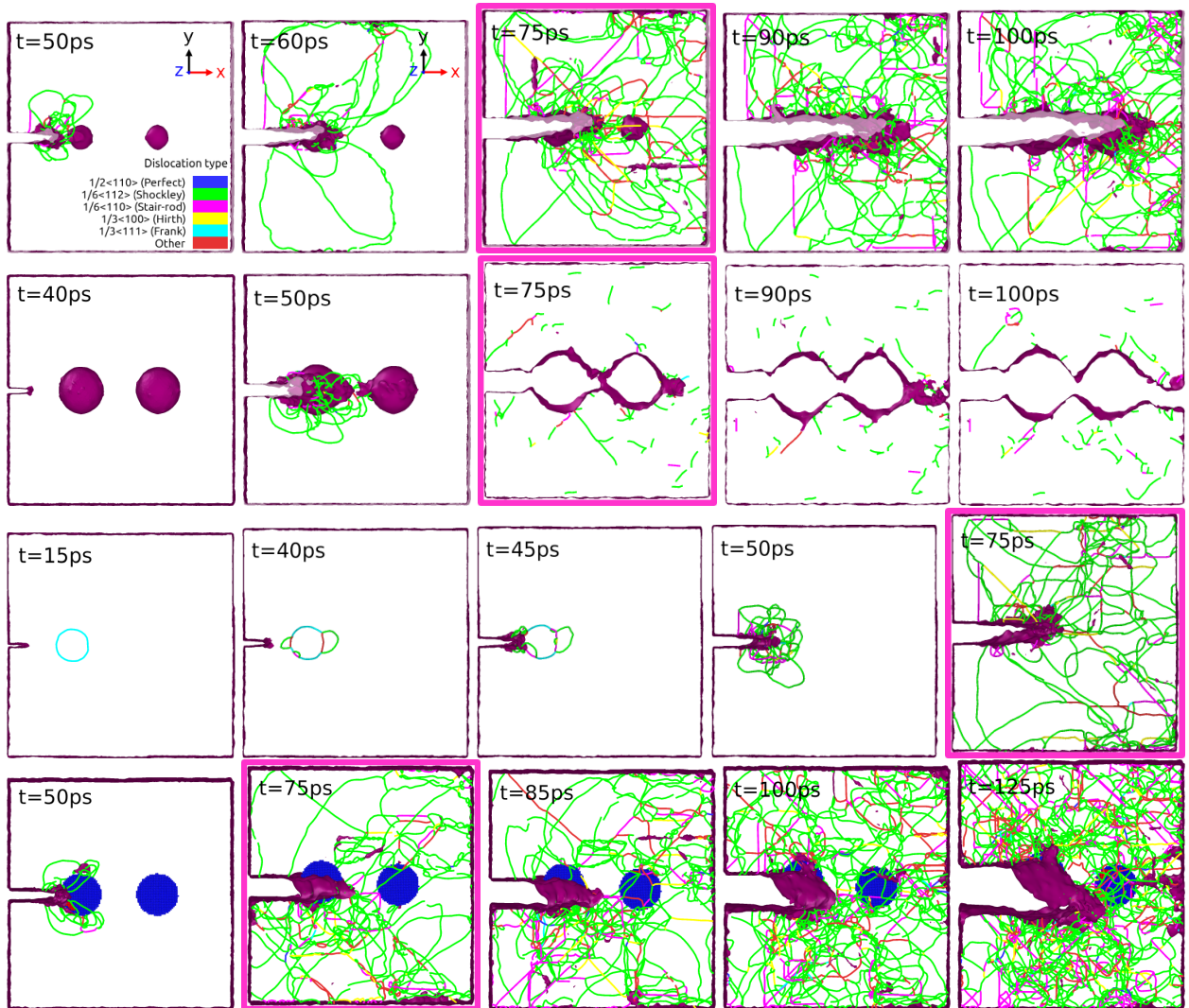


**Figure 10:** Fundamental mechanisms of a single defect–crack interaction governing crack propagation. Frames outlined in pink correspond to the same moment in time (75ps).

controlled configurations enabled a systematic exploration of the effects of defect size and type on crack propagation.

In the first row of Fig. 10, the crack approaches two small voids, each with a diameter of 2.5 nm. These voids act as localized weak points in the material, reducing the effective cohesive energy and creating regions of lower fracture resistance. As the crack propagates, it preferentially connects to these voids, accelerating crack growth. This mechanism highlights how voids act as stress concentrators, lowering the energy barrier for crack propagation and promoting fracture along paths of least resistance [47–49].

In the second row of Fig. 10, the crack approaches two larger voids, each with a diameter of 5 nm. Due to the increased size, these voids have a more pronounced effect on crack propagation, creating a disruption in the crack’s path as it merges with the voids. This interaction accelerates the crack propagation as the crack incorporates the void regions into its path.

In the third row of Fig. 10, the crack interacts with a dislocation loop spanning 5 nm. This interaction is distinct because the dislocation loop acts as a barrier, impeding crack growth by obstructing dislocation

motion. As the crack encounters the dislocation loop, it experiences increased resistance, which can alter its trajectory or even temporarily halt its progression. The presence of the dislocation loop leads to localized stress concentrations around the crack front, which can enhance dislocation emission and create complex dislocation structures near the crack tip.

In the fourth row of Fig. 10, the crack faces two rigid inclusions, each with dimensions of 5 nm. The rigid inclusions are introduced through the application of boundary conditions that constrain any deformation within the inclusion region during the simulation, thereby ensuring the inclusion remains a fixed, immovable obstacle within the material. These inclusions represent strong obstacles that divert the crack path, leading to a more tortuous and irregular morphology. Unlike voids, which weaken the material locally, rigid inclusions increase local resistance and force the crack to change direction, often leading to stress concentration at points where the crack path is redirected. This can result in additional dislocation activity around the inclusions as the crack adapts to the path of least resistance. This results in a more tortuous and branched crack morphology.

Fig. 10 presents the interplay between crack dynamics and radiation-induced defects, revealing how defect size, type, and spatial distribution shape crack behavior. This analysis emphasizes the dual role of defects in either facilitating or obstructing crack propagation, depending on their nature. The examples examined highlight the transition from crack paths governed by localized weakening, as seen with voids, to trajectories shaped by resistance and redirection due to dislocation loops or rigid inclusions.

### 3.3. Summary of defect-driven fracture mechanisms in irradiated materials

This section presents a detailed summary of the mechanisms governing crack propagation in irradiated materials, as revealed by the MD simulations reported above, emphasizing the complex interactions between radiation-induced defects and fracture dynamics. The results highlight the complexity of mechanisms that dictate fracture behavior, providing fundamental insights into the competing factors of crack growth. The key findings are summarized as follows:

- Mechanism of void–crack interactions: Voids act as local weak points in the material, reducing the effective energy and creating pathways of reduced resistance for crack growth. In regions with high void concentrations, the crack propagates more easily, as the voids lower the local stress required for atomic bond breaking. This mechanism is particularly pronounced when voids coalesce ahead of the crack tip, forming larger voids that further weaken the material. The coalescence of voids not only accelerates crack propagation but also leads to irregular crack morphologies, as the crack tends to follow the path of least resistance through these weakened zones. This process often results in crack branching, where the primary crack splits into multiple secondary cracks, increasing the overall fracture surface area and contributing to a more complex fracture pattern.
- Mechanism of dislocation loop–crack interactions: In contrast to voids, dislocation loops act as barriers to crack propagation. These loops, formed from clusters of interstitial atoms that form stable structures, obstruct the motion of dislocations near the crack tip, creating localized stress concentrations. When the crack encounters a dislocation loop, its progression is temporarily halted. This interaction can lead to the emission of additional dislocations from the crack tip, promoting localized plastic deformation and energy dissipation. However, in irradiated materials, the mobility of these dislocations is significantly restricted by the presence of other radiation-induced defects, such as voids and additional dislocation loops. As a result, the energy dissipation through plasticity is reduced, and the material becomes more prone to brittle fracture. Notably, dislocation loops, due to their immobile nature, can also act similarly to rigid inclusions by deflecting crack paths, increasing local stress concentrations, and altering crack propagation trajectories.

- Radiation-induced defects as nucleation sites for dislocations: In addition to acting as obstacles, irradiation-induced defects serve as preferential nucleation sites for dislocation formation. Defect clusters, such as voids and dislocation loops, introduce local stress concentrations that facilitate dislocation emission. As irradiation levels increase, dislocation nucleation leads to reduced plasticity and a more brittle fracture response. This dual role of defects, both as dislocation sources and barriers, critically influences the balance between ductile and brittle failure mechanisms.
- Mechanism of amorphous zone development at the crack tip: The amorphous zones which consist of disordered atomic structures form as a result of the accumulation of radiation-induced defects, such as dislocation loops. These zones, act as barriers to crack propagation, absorbing energy and temporarily halting the crack's advance. However, these zones also contribute to localized embrittlement, as the disordered structure reduces the material's ability to deform plastically. As a result, the secondary cracks can be formed, further increasing the complexity of the fracture process.
- Crack branching and secondary crack formation: High defect densities, particularly clusters of dislocation loops, lead to crack branching and the initiation of secondary cracks. When the primary crack encounters dense defect fields, it can branch or form secondary cracks, which eventually coalesce with the main crack. This results in irregular fracture patterns and an increased fracture surface area. The formation of secondary cracks is driven by the stress concentrations around radiation-induced defects, which provide initiation sites for new cracks.

The fracture behavior of irradiated materials is governed by a complex and interconnected interplay of mechanisms, including void–crack interactions, dislocation loop–crack interactions, rigid inclusions, amorphous zone formation, void coalescence, crack branching, and stress concentration effects. These mechanisms are not isolated; they are often coupled and interlocked in specific regions and under certain conditions, creating a highly dynamic and interdependent fracture process.

By examining each mechanism individually, a clearer understanding of its specific role in the fracture process can be obtained. However, it is only through the collective analysis of these mechanisms that the complexity of fracture dynamics in irradiated materials can be fully comprehended. Together, these mechanisms determine the crack trajectory, propagation velocity, and overall fracture morphology. The material's ability to dissipate energy through plasticity is significantly altered by the presence of radiation-induced defects, leading to a transition from ductile to brittle fracture. This transition is driven by the combined effects of defect interactions, which reduce the material's capacity for plastic deformation and promote brittle failure modes.

## 4. Analysis of the critical strain energy release rate

### 4.1. Framework for energy-based fracture analysis

In brittle fracture, the energy expended in the fracture process primarily goes into creating two new surfaces, where atomic bonds are broken. The energy needed for crack growth to overcome the cohesive forces between atoms corresponds to increased surface energy supplied by the elastic strain energy stored in the material. The classical Griffith theory defines the critical energy release rate as  $G_c = 2\gamma_s$ , where  $\gamma_s$  represents the fracture surface energy, assuming purely brittle propagation with energy dissipation confined to the creation of new free surfaces.

However, in materials where crack extension is accompanied by plastic deformation, the Griffith framework becomes insufficient. The works by Orowan [50], Jokl et al. [51] and Beltz and Rice [52] established that energy dissipation during fracture involves both bond-breaking and plastic work  $w_p$  from

dislocation nucleation and slip. Jokl et al. [51] derived a thermodynamic criterion reformulating the critical energy release rate as:

$$G_c = 2\gamma_s + w_p, \quad (1)$$

where  $\gamma_s$  represents the fracture surface energy and  $w_p$  is the plastic work per unit crack area due to dislocation activity. Concurrently, Beltz and Rice [52] analyzed the competition between cleavage and dislocation nucleation at crack tips, introducing the concept of an unstable stacking energy as the barrier for dislocation emission. Together, these works provided a foundation for computing  $G_c$  in materials where plasticity and defects govern fracture.

Recent advances by Xu and Demkowicz [20] have applied this framework to atomistic simulations, directly calculating the critical energy release rate  $G_c$  for systems with crack-tip plasticity. It has been shown that  $w_p$  depends on the sample size, which is strongly limited in MD due to computational cost. In this approach,  $G_c$  is defined as the increment of the total dissipated energy,  $dE_{\text{dis}}$ , per increment of the projected crack surface area,  $dA_{\text{crack}}$ , thus

$$G_c = \frac{\partial E_{\text{dis}}}{\partial A_{\text{crack}}} \approx \frac{dW - dU}{dA_{\text{crack}}}. \quad (2)$$

Here, referring to the MD simulations, the dissipated energy increment  $dE_{\text{dis}} = dW - dU$  is determined as the difference between the increments of the internal energy  $U$  (comprising potential and kinetic energies) and external work  $W$  (derived from the stress–strain response). Note that, under isothermal conditions, the dissipated energy corresponds to the change in Helmholtz free energy,  $dE_{\text{dis}} = dW - dF$  were  $dF = dU - TdS$ , which includes contributions from both internal energy  $U$  and entropy  $S$ . Above, the entropy contribution has been disregarded.

Moreover, for processes maintained at constant temperature, which define the scope of this analysis, the total dissipated energy reflects contributions from both bond rupture and plastic deformation. In the MD framework applied here, the thermostat regulates temperature by dynamically adjusting atomic velocities to dissipate excess kinetic energy generated during plastic work. This ensures the system remains at constant temperature ( $T=\text{constant}$ ), isolating mechanical contributions to  $dE_{\text{dis}} = dW - dU$ .

## 4.2. Effects of irradiation on fracture energy

Irradiation-induced defects fundamentally alter fracture behavior by degrading atomic cohesion (which influences surface energy,  $\gamma_s$ ) and suppressing dislocation-mediated plasticity (which impacts plastic work,  $w_p$ ). The spatial distribution, size, and density of these defects govern their collective impact on fracture resistance, creating a microstructure-dependent competition between brittle crack propagation and energy absorption through plastic deformation.

The critical energy release rate  $G_c$  is therefore explicitly controlled by the radiation dose (dpa), which specifies defect density, with temperature  $T$  serving here as a secondary parameter to isolate thermal activation of plasticity, thus:

$$G_c(\text{dpa}, T) = 2\gamma_s(\text{dpa}, T) + w_p(\text{dpa}, T). \quad (3)$$

Note that temperature modulates  $w_p$  through thermally activated dislocation glide, a defining feature of temperature-driven DBT. In contrast, the irradiation-driven DBT investigated here is dominated by radiation-induced defects that inhibit dislocation mobility and thereby fundamentally alter  $w_p$ .

To estimate the intrinsic surface energy  $\gamma_s(\text{dpa}, T)$ , first the separation energy  $2\gamma_{\text{sep}}(\text{dpa}, T)$  is considered, as a lower bound:

$$2\gamma_s(\text{dpa}, T) \geq 2\gamma_{\text{sep}}(\text{dpa}, T). \quad (4)$$

Here,  $\gamma_{\text{sep}}$  represents a lower estimate of the surface energy because it corresponds to an idealized surface created under perfect conditions rather than the actual surface resulting from the fracture process.

An upper bound for  $\gamma_s$  can be obtained independently from the critical energy release rate at absolute zero temperature ( $T = 0\text{K}$ ), where thermal activation is suppressed and plastic dissipation is limited ( $w_p \approx 0$ ):

$$2\gamma_s(\text{dpa}, T) \leq G_c(\text{dpa}, 0\text{K}). \quad (5)$$

Finally, at finite temperatures ( $T > 0\text{K}$ ), the temperature-dependent plastic work term,  $w_p(\text{dpa}, T)$ , can be estimated as:

$$w_p(\text{dpa}, T) = G_c(\text{dpa}, T) - 2\gamma_s(\text{dpa}, T), \quad 2\gamma_{\text{sep}}(\text{dpa}, T) \leq 2\gamma_s(\text{dpa}, T) \leq G_c(\text{dpa}, T). \quad (6)$$

Eq. (6) isolates the energy dissipated by dislocations as they interact with radiation-induced defects, providing a direct measure of the material's plastic response to irradiation.

The radiation-induced ductile-to-brittle transition can be characterized by a decrease in  $w_p(\text{dpa}, T)$  as the radiation dose (dpa) increases. Radiation-induced defects affect dislocation motion, altering the balance between plasticity and bond rupture during crack propagation (see Section 3.3). The following regimes can be identified based on the value of  $w_p(\text{dpa}, T)$ :

- *high  $w_p(\text{dpa}, T)$  – ductile regime*: plasticity dominates, and dislocations play a crucial role in shielding the crack tip;
- *low  $w_p(\text{dpa}, T)$  – brittle regime*: defect-induced hardening significantly restricts dislocation motion, leaving the crack tip unshielded and causing crack propagation to occur primarily through bond rupture, leading to a more brittle fracture response.

### 4.3. Energy dissipation in irradiated materials

In this subsection, the mechanisms of energy dissipation during crack propagation in irradiated materials are investigated across varying radiation doses, drawing on the MD simulation results presented in Section 3. By analyzing the interplay between internal energy  $U$ , external work  $W$ , and stress–strain behavior, the influence of defect populations on the critical energy release rate  $G_c$  and the balance between surface energy  $\gamma_s$  and plastic work dissipation  $w_p$  is quantified.

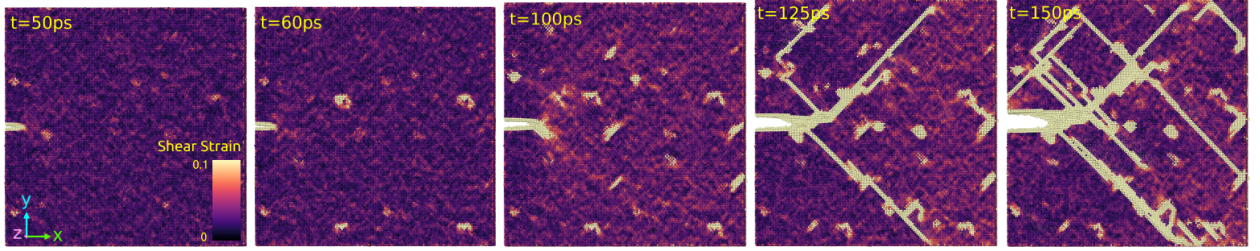
In order to evaluate the plastic work  $w_p(\text{dpa}, T)$  as defined in Eq. (6), the critical energy release rate  $G_c(\text{dpa}, 0\text{K})$  should be determined at absolute zero temperature. To pragmatically approximate  $G_c(\text{dpa}, 0\text{K})$ , a finite simulation temperature of  $T=10\text{K}$  is employed.

$$G_c(\text{dpa}, 10\text{K}) \approx G_c(\text{dpa}, 0\text{K}). \quad (7)$$

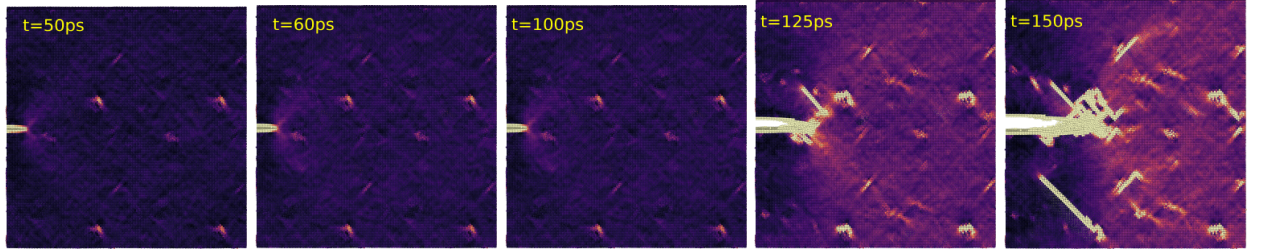
This temperature is sufficiently low to suppress thermally activated processes, thereby preserving the near-brittle fracture conditions required for isolating the surface energy contribution according to Eq. (6). Thus, by evaluating fracture energy at two distinct temperature levels, the contribution of plastic work to energy dissipation can be effectively isolated. The low-temperature condition serves as a near-brittle reference state, minimizing dislocation activity and allowing the surface energy component to be approximated. In contrast, at higher temperatures, where plastic deformation mechanisms are active, the additional energy dissipation due to dislocation motion can be quantified.

Fig. 11 compares the equivalent shear strain fields, calculated similarly to Fig. 6, in cross-sections of samples irradiated to 0.07 dpa at 300K and 10K. At 300K (top row), the strain field exhibits a more widespread distribution than 10K (bottom row), with deformation occurring throughout the sample and strain localizing particularly around the crack and radiation-induced defects. This reflects thermally activated

T=300K; sample irradiated to 0.07 dpa



T=10K; sample irradiated to 0.07 dpa



**Figure 11:** Equivalent shear strain fields calculated using the Green–Lagrangian strain tensor [37] in a selected cross-section of the samples irradiated to 0.07 dpa at 300K and 10K.

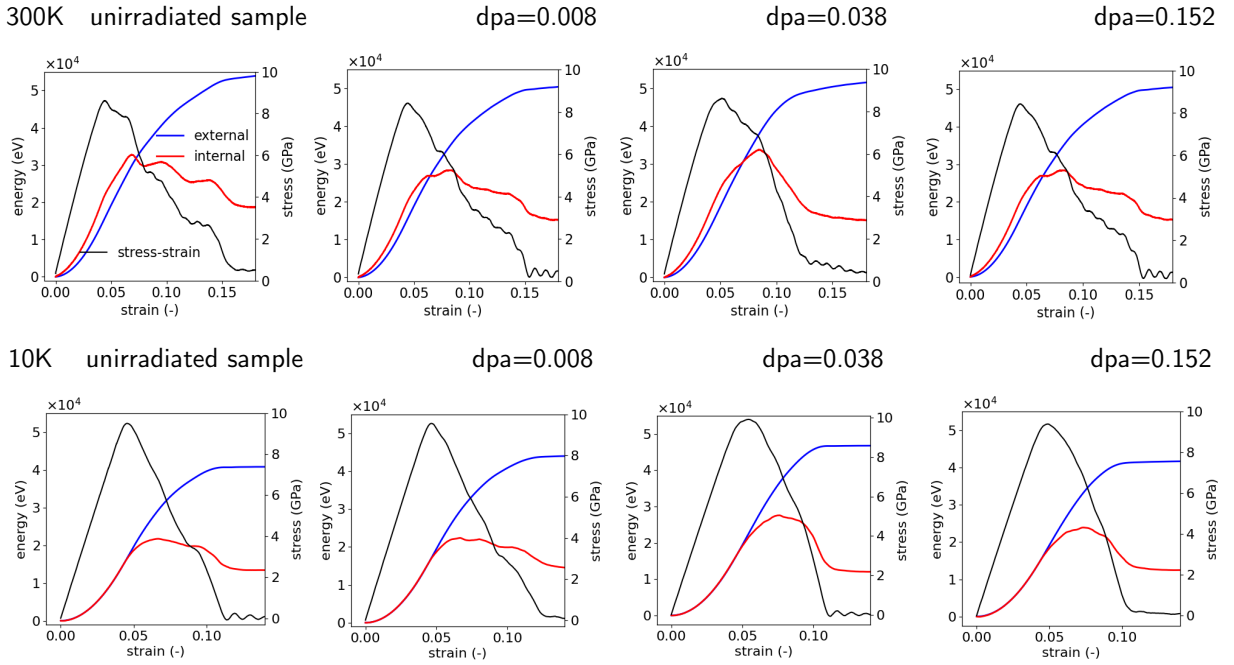
dislocation motion, which enables plasticity and contributes to energy dissipation. In contrast, at 10K (bottom row), the strain is highly concentrated around the crack tip and radiation defects, with minimal deformation in the surrounding material. The suppression of strain outside these localized regions indicates restricted dislocation mobility and reduced plasticity, leading to more brittle fracture behavior. This comparison demonstrates that separation energy  $\gamma_{\text{sep}}$  and simulations at 10K can serve as a near-brittle reference state for approximating  $G_c(\text{dpa}, 0\text{K})$  in Eq. (6).

The effectiveness of this framework is demonstrated below through a detailed examination of energy dissipation characteristics in irradiated materials.

The evolution of internal energy  $\Delta U = U - U_0$  (red curve) with  $U_0$  referring to the initial reference state, external work  $W$  (blue curve), and stress–strain response (black curve) for unirradiated and irradiated samples (0.008, 0.038, and 0.152 dpa) at two different temperatures, 300K and 10K are shown in Fig. 12. At 300K, all samples exhibit discrete steps in their post-peak stress–strain curves, corresponding to crack arrest at the knots of entangled dislocations (compare Fig. 9 and Section 3). These steps are also evident in the internal energy curve, reflecting energy relocation (or redistribution) as it diverts (or shifts) from bond rupture to dislocation nucleation. The unirradiated sample displays a characteristic post-yield plateau (Fig. 12, top-left), indicative of homogeneous plastic zone development through unimpeded dislocation motion. Irradiation disrupts this plasticity: especially visible at 0.008 and 0.152 dpa, the stress drops abruptly after yielding, indicating defect-dominated fracture driven by crack-void interactions with limited plastic dissipation (compare Section 3).

It is worth noting that the discrepancy between internal energy  $\Delta U$  and external work  $W$  in the elastic deformation regime, where  $\Delta U$  marginally exceeds  $W$ , arises from the thermostat's enforcement of isothermal conditions under the NVT ensemble. In fact, from the energy balance, the difference,  $Q = \Delta U - W$ , is the heat supplied to the system by the thermostat, which is positive ( $Q > 0$ ) in the elastic deformation regime. Once inelastic deformation mechanisms initiate (for the overall strain exceeding  $\sim 0.04$ ), the heat  $Q$  becomes negative ( $Q < 0$ ), i.e., heat is taken from the system by the thermostat.

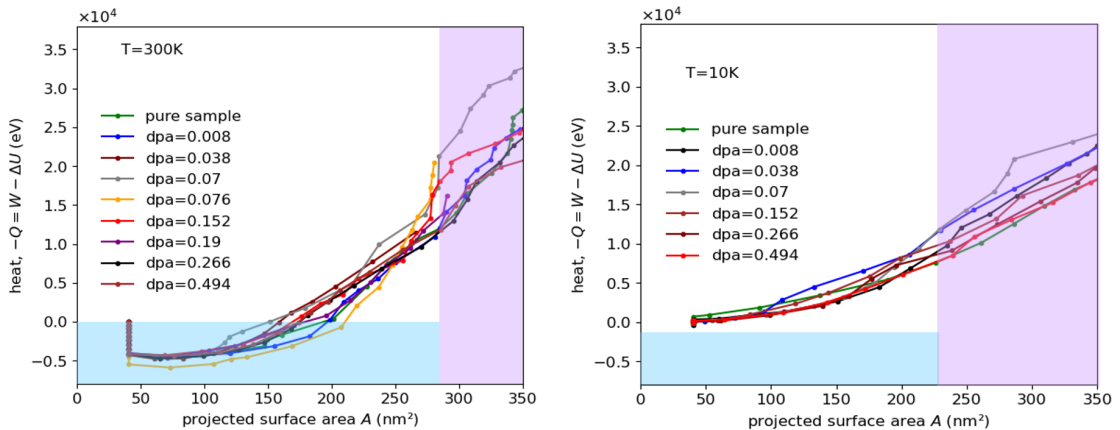
## Ductile-to-Brittle Transition



**Figure 12:** Stress–strain curves and energy evolution for different irradiation levels at 300 K and 10 K, showing internal energy  $\Delta U$  (red), external work  $W$  (blue), and stress–strain response (black).

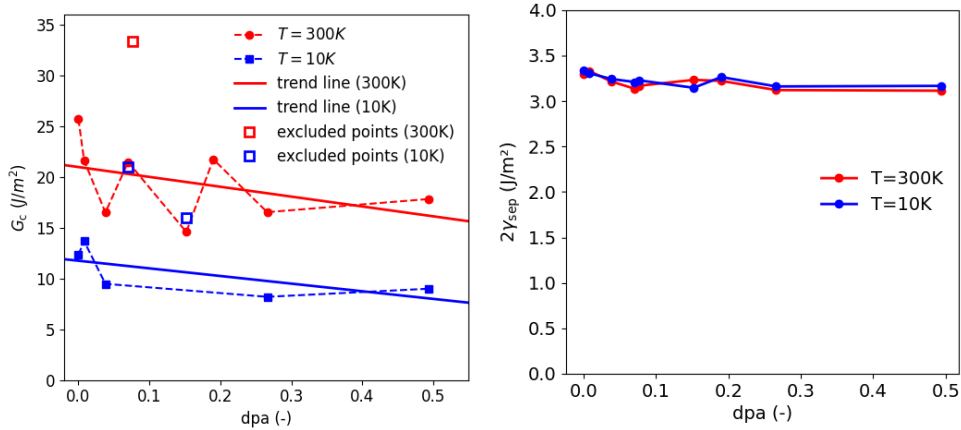
At 10K, the energy profiles and stress–strain behavior display a distinctly different response compared to 300 K, reflecting the reduced atomic mobility and increased brittleness at low temperatures. In particular, at this temperature, internal energy closely follows external work during the elastic deformation stage and the heat supplied to the system is then negligible.

Fig. 13 shows the heat taken from the system ( $-Q = W - \Delta U$ ) as a function of the projected crack surface area  $A$  for all samples considered. Here,  $W$  and  $\Delta U$  correspond to those shown in Fig. 12, while the surface area  $A$  represents the two-dimensional geometric projection of the crack's surface onto the  $x$ - $z$



**Figure 13:** Heat taken from the system ( $-Q = W - \Delta U$ ) as a function of projected crack surface area  $A$  for a wide dpa range at (a) 300K and (b) 10K.

## Ductile-to-Brittle Transition



**Figure 14:** (a) Critical energy release rate  $G_c$  as a function of irradiation level (dpa) at different temperatures: 300K (dashed red line) and 10K (dashed blue line), with solid lines indicating approximation curves. (b) Separation energy  $2\gamma_{\text{sep}}$  for crack surface formation as a function of dpa.

plane. Note that the initial drop of  $-Q$  in Fig. 13(a) corresponds to the elastic deformation stage at which the crack surface area remains unchanged at  $A = 40 \text{ nm}^2$ , while the heat is supplied to the system ( $Q > 0$ ), as discussed above with reference to Fig. 12.

By following the approach of Xu and Demkowicz [20], the dependence of  $-Q$  on  $A$  can now be used to determine the critical energy release rate  $G_c$ . Indeed, in the quasi-steady state crack propagation regime, the heat taken from the system by the thermostat corresponds to the energy dissipated as a result of crack propagation and dislocation activity, thus  $dE_{\text{dis}} = -dQ$ . For each sample,  $G_c$  can thus be determined as the slope of the corresponding curve in Fig. 13 according to Eq. (2). Note that the initial stage (marked in blue) and the final stage (marked in purple) are excluded from calculations. The transient initial stage corresponds to the build-up of the plastic zone ahead of the crack tip. The final stage is omitted because of the direct interaction of the crack front with the boundary of the simulation box.

Fig. 14(a) presents the critical energy release rate,  $G_c$ , determined according to Eq. (2), as a function of irradiation level (dpa) at two different temperatures:  $T=300\text{K}$  (red markers) and  $T=10\text{K}$  (blue markers). The solid lines represent linear approximations of these trends. The extreme values of  $G_c$  (denoted by empty squares) are excluded to emphasize the dominant irradiation-driven trends. These correspond to cases where the crack encounters strong obstacles, such as entangled dislocations (compare Fig. 9), which hinder its propagation and result in anomalously high fracture energy values. Fig. 14(a) shows that  $G_c$  decreases with increasing dpa, indicating a reduction in the material's resistance to fracture as irradiation damage accumulates. Fig. 14(b) shows the separation energy  $2\gamma_{\text{sep}}$  as a function of dpa, defined as the energy required to break atomic bonds and create two fracture surfaces in the absence of plastic deformation. This parameter serves as a reference point for intrinsic surface energy and offers additional insight into the interplay between defect density and fracture energy response. The overall values of  $2\gamma_{\text{sep}}$  at 300K and 10K remain comparable and show little variation with dpa, indicating that both temperature and irradiation have a small effect on the intrinsic separation energy in the absence of significant plastic deformation.

The results show a trend consistent with an irradiation-induced ductile-to-brittle transition. At  $T=300\text{K}$ ,  $G_c$  decreases over the examined dpa range, indicating suppressed energy dissipation mechanisms as defect density increases. The higher  $G_c$  at 300K is attributed to thermally activated processes that allow some dislocation-mediated energy absorption. At  $T=10\text{K}$ ,  $G_c$  moves closer to the theoretical limit governed by

## Ductile-to-Brittle Transition

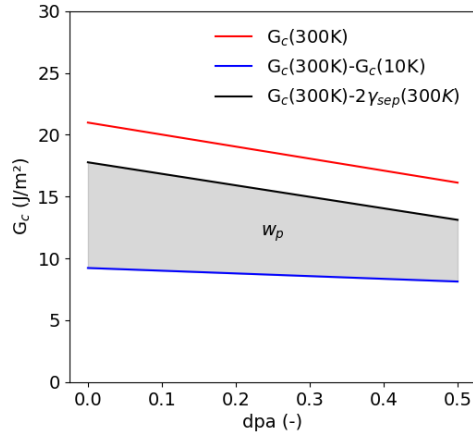


**Figure 15:** Plastic work,  $w_p$ , as a function of the irradiation dose. The red curve represents  $G_c(300K)$ , the blue curve shows the difference between the total critical energy release rate at  $T=300K$  and the critical energy release rate at  $T=10K$ , and the black curve denotes  $G_c(300K) - 2\gamma_{sep}(300K)$ , see Fig. 14. The shaded region highlights the estimated range of values of the plastic work,  $w_p$ .

intrinsic surface energy  $\gamma_{sep}$  (Fig. 14(b)), as the lack of thermal energy prevents significant dislocation motion, making bond rupture the predominant fracture mechanism.

Fig. 15 is derived from the data presented in Fig. 14 (only linear trend lines are shown) and illustrates the contribution of energy dissipation mechanisms as a function of irradiation level (dpa). The red curve represents  $G_c(300K)$ , which captures the total energy required for crack propagation at 300K. The blue curve, defined as  $G_c(300K) - G_c(10K)$  represents the lower bound of  $w_p$ , and the black curve defined as  $G_c(300K) - 2\gamma_{sep}(300K)$  represents the upper bound of  $w_p$ . The shaded region highlights the progressive reduction in energy dissipation,  $w_p$ , associated with dislocation-mediated processes as the irradiation dose increases. This reduction indicates the suppression of dislocation activity due to the accumulation of irradiation-induced defects.

## 5. Summary and discussion

This study provides a comprehensive investigation into the fracture behavior of irradiated Fe–Ni–Cr alloys, revealing how radiation-induced defects govern the transition from ductile to brittle failure. Although the system investigated in this study does not exhibit fully brittle failure due to the limited defect density inherent to the small MD sample size, the observed embrittlement trends offer valuable insights into the underlying mechanisms governing this transition.

The crack propagation behavior in irradiated materials is governed by a complex interplay of mechanisms, as detailed in Section 3.3. Voids act as weak zones that accelerate fracture through coalescence, reducing the cohesive energy and providing pathways for crack growth. Dislocation loops obstruct dislocation motion, redirecting cracks and promoting branching, which alters the crack path and increases fracture surface area. At higher irradiation levels, amorphous zones form at crack tips, suppressing plasticity and promoting a more brittle failure mode. High defect densities also lead to crack branching and the initiation of secondary cracks, which coalesce with the main crack, resulting in irregular fracture patterns. Additionally, radiation-induced defects generate localized stress concentrations, further influencing crack propagation and fracture morphology. These mechanisms collectively contribute to embrittlement, with the balance between plasticity and bond rupture shifting as irradiation damage accumulates.

Atomistic simulations and energy-based analysis demonstrate that irradiation embrittlement arises from the suppression of plasticity, driven by defect-mediated interactions that restrict dislocation motion and alter crack propagation. To quantify the material's diminishing capacity for plastic deformation under irradiation, we decompose the critical energy release rate,  $G_c$ , into two primary contributions: surface energy  $\gamma_s$ , which represents the energy required to create new fracture surfaces, and plastic work  $w_p$ , associated with dislocation motion and other inelastic deformations.

We estimate the surface energy  $\gamma_s$  using two approaches: one derived from the separation energy ( $2\gamma_{sep}$ ) and another from the critical energy release rate at low temperatures ( $G_c(10K)$ ), treated as the lower and upper bound of  $\gamma_s$ , respectively. At  $T=10K$ , where plasticity is suppressed,  $G_c(10K)$  provides an approximation of the near-brittle fracture limit. To determine the plastic work contribution, we compare the fracture energy at  $T=300K$ , where plasticity remains active, to the near-brittle reference state at  $T=10K$ . This allows us to isolate the energy dissipated through plastic deformation as irradiation-induced defects interact with dislocations. Ultimately, the plastic work contribution is specified using two complementary definitions.

This energy-based framework provides a generalizable approach to assessing embrittlement, independent of specific temperature values, as long as the chosen low-temperature condition captures near-brittle behavior while the high-temperature condition allows sufficient plasticity. The results reveal that irradiation progressively reduces plastic work, directly linking irradiation hardening to suppressed dislocation activity. This approach connects microstructural damage to macroscopic fracture resistance, offering a quantitative framework for evaluating fracture behavior in irradiated materials.

The study advances the field through three key contributions:

- *Defect-driven fracture pathways*: By categorizing crack-void and crack-loop interactions, we establish that voids accelerate fracture by reducing cohesive strength, while loops impede propagation by pinning dislocations. This duality explains the transition from ductile tearing to brittle cleavage as dpa increases.
- *Microstructural-mechanical linkage*: The correlation between defect density, crack morphology, and energy dissipation bridges atomic-scale simulations to macroscopic fracture resistance, offering a unified model for irradiation embrittlement.
- *Energy-based embrittlement criterion*: Building on Xu and Demkowicz [20], we adapt the decomposition of  $G_c$  into brittle ( $\gamma_s$ ) and plastic ( $w_p$ ) contributions for irradiated materials. This framework provides a step toward quantifying how irradiation affects the fracture energy balance.
- *Quantitative description of irradiation-induced DBT*: The study demonstrates a decrease in both  $G_c$  and  $w_p$  with increasing dpa, providing a quantitative manifestation of irradiation-induced ductile-to-brittle transition. While the observed embrittlement is relatively small due to the limited dpa range in our MD simulations, real-world scenarios with higher dpa values and greater defect densities are expected to exhibit more pronounced DBT effects.

## Acknowledgments

The National Science Centre in Poland supports this work through Grant No UMO-2020/38/E/ST8/00453. FJDG acknowledges partial support from the European Union Horizon 2020 research and innovation program under grant agreement No. 857470 and from the European Regional Development Fund via the Foundation for Polish Science International Research Agenda PLUS program grant No. MAB PLUS/2018/8. We gratefully acknowledge Polish high-performance computing infrastructure PLGrid (HPC Center at ACK Cyfronet AGH) for providing computer facilities and support within computational Grant No.

PLG/2024/017084 and the CIS High Performance Cluster at the National Centre for Nuclear Research in Poland.

## References

- [1] M. J. Norgett, M. T. Robinson, and I. M. Torrens. A proposed method of calculating displacement dose rates. *Nuclear Engineering and Design*, 33(1):50–54, 1975.
- [2] H. Krull and H. Yuan. Suggestions to the cohesive traction–separation law from atomistic simulations. *Engineering Fracture Mechanics*, 78(3):525–533, 2011. Meso-Mechanical Modelling of Fatigue and Fracture.
- [3] F. Granberg, K. Nordlund, Mohammad W. Ullah, K. Jin, C. Lu, H. Bei, L. M. Wang, F. Djurabekova, W. J. Weber, and Y. Zhang. Mechanism of radiation damage reduction in equiatomic multicomponent single phase alloys. *Phys. Rev. Lett.*, 116:135504, Apr 2016.
- [4] K. Nordlund, S. J. Zinkle, A. E. Sand, F. Granberg, R. S. Averback, R. E. Stoller, T. Suzudo, L. Malerba, F. Banhart, W. J. Weber, F. Willaime, S. L. Dudarev, and D. Simeone. Primary radiation damage: A review of current understanding and models. *Journal of Nuclear Materials*, 512:450–479, 2018.
- [5] Y. Li, X. Ren, J. He, and Z. Zhang. Constraint effect on the brittle-to-ductile transition of single-crystal iron induced by dislocation mobility. *International Journal of Mechanical Sciences*, 149:212–223, 2018. ISSN 0020-7403.
- [6] R. Barik, A. Ghosh, and D. Chakrabarti. Fundamental insights on ductile to brittle transition phenomenon in ferritic steel. *Materialia*, 27:101667, 2023.
- [7] R. Barik, T. Jayasree, A. Biswal, S. and Ghosh, and D. Chakrabarti. Investigating the ductile to brittle transition phenomenon in binary fe-ni systems using molecular dynamics simulation. *Journal of the Mechanics and Physics of Solids*, 187:105624, 2024.
- [8] P. Lin, J. F. Nie, S. G. Cui, and Y. P. Lu. Molecular dynamics study on the ductile-to-brittle transition in w-re alloy systems. *Acta Materialia*, 285:120684, 2025.
- [9] Y. Cheng, Z. H. Jin, Y. W. Zhang, and H. Gao. On intrinsic brittleness and ductility of intergranular fracture along symmetrical tilt grain boundaries in copper. *Acta Materialia*, 58(7):2293–2299, 2010.
- [10] J. J. Möller and E. Bitzek. On the influence of crack front curvature on the fracture behavior of nanoscale cracks. *Engineering Fracture Mechanics*, 150:197–208, 2015.
- [11] T.S. Byun, K. Farrell, E.H. Lee, L.K. Mansur, S.A. Maloy, M.R. James, and W.R. Johnson. Temperature effects on the mechanical properties of candidate sns target container materials after proton and neutron irradiation. *Journal of Nuclear Materials*, 303:34–43, 2002.
- [12] A. Ustrzycka, F.J. Dominguez-Gutierrez, and W. Chromiński. Atomistic analysis of the mechanisms underlying irradiation-hardening in fe–ni–cr alloys. *International Journal of Plasticity*, 182:104118, 2024.
- [13] T. S. Byun, K. Farrell, E. H. Lee, J. D. Hunn, and L. K. Mansur. Strain hardening and plastic instability properties of austenitic stainless steels after proton and neutron irradiation. *Journal of Nuclear Materials*, 298:269–279, 2001.
- [14] Chi. Ji, J. Hu, Z. Zhuang, and Y. Cui. Atomistically-informed hardening and kinetics models of helium bubble in irradiated tungsten. *International Journal of Plasticity*, 165:103620, 2023.
- [15] Yu.N. Osetsky, R.E. Stoller, and Y. Matsukawa. Dislocation–stacking fault tetrahedron interaction: what can we learn from atomic-scale modelling. *Journal of Nuclear Materials*, 329–333:1228–1232, 2004.
- [16] Y. Cui, G. Po, and N. Ghoniem. Does irradiation enhance or inhibit strain bursts at the submicron scale? *Acta Materialia*, 132:285–297, 2017.
- [17] H. Bao, H. Xu, Y. Li, H. Bai, and F. Ma. The interaction mechanisms between dislocations and nano-precipitates in cufe alloys: A molecular dynamic simulation. *International Journal of Plasticity*, 155:

103317, 2022.

- [18] T. Tsugawa, S. Hayakawa, Y. Iwase, T. Okita, K. Suzuki, M. Itakura, and M. Aichi. Molecular dynamics simulations to quantify the interaction of a rigid and impenetrable precipitate with an edge dislocation in cu. *Computational Materials Science*, 210:111450, 2022.
- [19] J. Zhang and S. Ghosh. Molecular dynamics based study and characterization of deformation mechanisms near a crack in a crystalline material. *Journal of the Mechanics and Physics of Solids*, 61(8):1670–1690, 2013.
- [20] G.Q. Xu and M.J. Demkowicz. Computing critical energy release rates for fracture in atomistic simulations. *Computational Materials Science*, 181:109738, 2020.
- [21] L. Wang, Q. Liu, and S. Shen. Effects of void–crack interaction and void distribution on crack propagation in single crystal silicon. *Engineering Fracture Mechanics*, 146:56–66, 2015.
- [22] R. W. Fuller, J. Simsiriwong, and N. Shamsaei. Crack growth prediction for irradiated stainless steels under the combined fatigue-creep loading. *Theoretical and Applied Fracture Mechanics*, 109:102759, 2020.
- [23] G. Xie, F. Wang, X. Lai, Z. Xu, and Z. Zeng. Atomistic study on crystal orientation-dependent crack propagation and resultant microstructure anisotropy in niti alloys. *International Journal of Mechanical Sciences*, 250:108320, 2023.
- [24] H. Ullmaier and Carsughi F. Radiation damage problems in high power spallation neutron sources. *Nuclear Instruments and Methods in Physics Research Section B: Beam Interactions with Materials and Atoms*, 101(4):406–421, 1995.
- [25] P. Chowdhury and H. Sehitoglu. Mechanisms of fatigue crack growth – a critical digest of theoretical developments. *Fatigue & Fracture of Engineering Materials & Structures*, 39:652–674, 2016.
- [26] B. Skoczeń and A. Ustrzycka. Kinetics of evolution of radiation induced micro-damage in ductile materials subjected to time-dependent stresses. *International Journal of Plasticity*, 80:86–110, 2016.
- [27] Weiming Ji and Mao See Wu. Atomistic studies of ductile fracture of a single crystalline cantor alloy containing a crack at cryogenic temperatures. *Engineering Fracture Mechanics*, 258:108120, 2021.
- [28] F.J. Domínguez-Gutiérrez and Udo von Toussaint. On the detection and classification of material defects in crystalline solids after energetic particle impact simulations. *Journal of Nuclear Materials*, 528:151833, 2020.
- [29] U. Toussaint, F.J. Dominguez-Gutierrez, M. Compostella, and M. Rampp. FaVAD: A software workflow for characterization and visualizing of defects in crystalline structures. *Computer Physics Communications*, 262:107816, 2021.
- [30] F. J. Dominguez-Gutierrez, A. Ustrzycka, Q. Q. Xu, R. Alvarez-Donado, S. Papanikolaou, and M. J. Alava. Dislocation nucleation mechanisms during nanoindentation of concentrated FeNiCr alloys: unveiling the effects of cr through molecular simulations. *Modelling and Simulation in Materials Science and Engineering*, 30(8), 2022. URL [www.scopus.com](http://www.scopus.com).
- [31] A. P. Thompson, H. M. Aktulga, R. Berger, D. S. Bolintineanu, W. M. Brown, P. S. Crozier, P. J. in 't Veld, A. Kohlmeyer, S. G. Moore, T. D. Nguyen, R. Shan, M. J. Stevens, J. Tranchida, C. Trott, and S. J. Plimpton. LAMMPS - a flexible simulation tool for particle-based materials modeling at the atomic, meso, and continuum scales. *Comp. Phys. Comm.*, 271:108171, 2022. doi: 10.1016/j.cpc.2021.108171.
- [32] G. Bonny, D. Terentyev, R. C. Pasianot, S. Poncé, and A. Bakaev. Interatomic potential to study plasticity in stainless steels: the fenicr model alloy. *Modelling and Simulation in Materials Science and Engineering*, 19:085008, 2011.
- [33] G. Bonny, N. Castin, and D. Terentyev. Interatomic potential for studying ageing under irradiation in stainless steels: the FeNiCr model alloy. *Modelling and Simulation in Materials Science and Engineering*, 21(8):085004, oct 2013.

- [34] L. K. Béland, A. Tamm, S. Mu, G. D. Samolyuk, Y. N. Osetsky, A. Aabloo, M. Klintonberg, A. Caro, and R. E. Stoller. Accurate classical short-range forces for the study of collision cascades in fe–ni–cr. *Computer Physics Communications*, 219:11–19, 2017.
- [35] X. Zhou, M. E. Foster, and R. B. Sills. Enabling molecular dynamics simulations of helium bubble formation in tritium-containing austenitic stainless steels: An fe-ni-cr-h-he potential. *Journal of Nuclear Materials*, 575:154232, 2023.
- [36] Alexander Stukowski. Visualization and analysis of atomistic simulation data with OVITO—the Open Visualization Tool. *Modelling and simulation in materials science and engineering*, 18(1), JAN 2010. ISSN 0965-0393. doi: {10.1088/0965-0393/18/1/015012}.
- [37] Alexander Stukowski. Visualization and analysis of atomistic simulation data with OVITO—the open visualization tool. *Modelling and Simulation in Materials Science and Engineering*, 18(1):015012, dec 2009.
- [38] D. Singh, P. Sharma, S. Jindal, P. Kumar, P. Kumar, and A. Parashar. Atomistic simulations to study crack tip behaviour in single crystal of bcc niobium and hcp zirconium. *Current Applied Physics*, 19(1): 37–43, 2019.
- [39] J. Ding, H. Zheng, Y. Tian, X. Huang, K. Song, S. Lu, X. Zeng, and W. Ma. Multi-scale numerical simulation of fracture behavior of nickel-aluminum alloy by coupled molecular dynamics and cohesive finite element method (cfem). *Theoretical and Applied Fracture Mechanics*, 109:102735, 2020.
- [40] M.J. Buehler. *Atomistic modeling of materials failure*. Springer, 2008.
- [41] M. Zhou. A new look at the atomic level virial stress: on continuum-molecular system equivalence. *Proceedings of the Royal Society of London. Series A: Mathematical, Physical and Engineering Sciences*, 459: 2347–2392, 2003.
- [42] V. Tvergaard. Void shape effects and voids starting from cracked inclusion. *International Journal of Solids and Structures*, 48(7):1101–1108, 2011.
- [43] I. Kawata, H. Nakai, and S. Aihara. Experimental evaluation of effective surface energy for cleavage microcrack propagation across grain boundary in steels. *Acta Materialia*, 150:40–52, 2018.
- [44] M. Boisson, L. Legras, E. Andrieu, and L. Laffont. Role of irradiation and irradiation defects on the oxidation first stages of a 316l austenitic stainless steel. *Corrosion Science*, 161:108194, 2019.
- [45] G. S. Was, C. B. Bahn, J. Busby, B. Cui, D. Farkas, M. Gussev, M. Rigen He, J. Hesterberg, Z. Jiao, D. Johnson, W. Kuang, M. McMurtrey, I. Robertson, A. Sinjlawi, M. Song, K. Stephenson, K. Sun, S. Swaminathan, M. Wang, and E. West. How irradiation promotes intergranular stress corrosion crack initiation. *Progress in Materials Science*, 143:101255, 2024.
- [46] N. Hytönen, S. Lindqvist, J. Lydman, Y. Ge, Z. Que, and P. Efsing. Microscopic characterisation of brittle fracture initiation in irradiated and thermally aged low-alloy steel welds of a decommissioned reactor pressure vessel. *Journal of Nuclear Materials*, 603:155423, 2025.
- [47] E. Bitzek and P. Gumbsch. Atomistic simulations of dislocation-crack interaction. *Journal of Solid Mechanics and Materials Engineering*, 2(10):1348–1359, 2008.
- [48] C Sagar, K. N. Naveen, M.K. Samal, V.M. Chavan, and R.J. Patel. Molecular dynamics simulations of crack growth behavior in al in the presence of vacancies. *Computational Materials Science*, 117:518–526, 2016.
- [49] L. Peng-tao, Y. Yan-qing, L. Xian, J. Na, L. Gang, F. Zong-qiang, et al. Effect of rate dependence of crack propagation processes on amorphization in al. *Materials Science and Engineering: A*, 684:71–77, 2017.
- [50] E. Orowan. *Notch Brittleness and the Strength of Metals*. Institution of Engineers and Shipbuilders in Scotland, 1945.
- [51] M. L. Jokl, V. Vitek, and C. J. McMahon. A microscopic theory of brittle fracture in deformable solids: A relation between ideal work to fracture and plastic work. *Acta Metallurgica*, 28(11):1479–1488, 1980.

- [52] G. E. Beltz and J. R. Rice. Dislocation nucleation at metal-ceramic interfaces. *Acta Metallurgica et Materialia*, 40:S321–S331, 1992. Proceedings of the International Symposium on Metal-Ceramic Interfaces.